



**HAL**  
open science

# **Anatomical connections in the human visual cortex: validation and new insights using a DTI Geodesic Connectivity Mapping method**

Nicolas Wotawa, Christophe Lenglet, Emmanuel Prados, Rachid Deriche,  
Olivier Faugeras

## ► To cite this version:

Nicolas Wotawa, Christophe Lenglet, Emmanuel Prados, Rachid Deriche, Olivier Faugeras. Anatomical connections in the human visual cortex: validation and new insights using a DTI Geodesic Connectivity Mapping method. [Research Report] RR-6176, 2007, pp.28. inria-00144016v1

**HAL Id: inria-00144016**

**<https://inria.hal.science/inria-00144016v1>**

Submitted on 30 Apr 2007 (v1), last revised 2 May 2007 (v2)

**HAL** is a multi-disciplinary open access archive for the deposit and dissemination of scientific research documents, whether they are published or not. The documents may come from teaching and research institutions in France or abroad, or from public or private research centers.

L'archive ouverte pluridisciplinaire **HAL**, est destinée au dépôt et à la diffusion de documents scientifiques de niveau recherche, publiés ou non, émanant des établissements d'enseignement et de recherche français ou étrangers, des laboratoires publics ou privés.



INSTITUT NATIONAL DE RECHERCHE EN INFORMATIQUE ET EN AUTOMATIQUE

*Anatomical connections in the human visual cortex:  
validation and new insights using a  
DTI Geodesic Connectivity Mapping method*

Nicolas Wotawa — Christophe Lenglet — Emmanuel Prados — Rachid Deriche — Olivier  
Faugeras

N° ????

April 2007

Thème BIO

 *rapport  
de recherche*





## **Anatomical connections in the human visual cortex: validation and new insights using a DTI Geodesic Connectivity Mapping method**

Nicolas Wotawa\*, Christophe Lenglet\*, Emmanuel Prados<sup>†</sup>, Rachid Deriche\*,  
Olivier Faugeras\*

Thème BIO — Systèmes biologiques  
Projets Odyssee

Rapport de recherche n° 7777 — April 2007 — 29 pages

**Abstract:** Various approaches have been introduced to infer the organization of white matter connectivity using Diffusion Tensor Imaging (DTI). In this study, we validate a recently introduced geometric tractography technique, Geodesic Connectivity Mapping (GCM), able to overcome the main limitations of geometrical approaches. Using the GCM technique, we could successfully characterize anatomical connections in the human low-level visual cortex. We reproduce previous findings regarding the topology of optic radiations linking the LGN to V1 and the regular organization of splenium fibers with respect to their origin in the visual cortex. Moreover, our study brings further insights regarding the connectivity of the human MT complex (hMT+) and the retinotopic areas.

**Key-words:** Diffusion tensor MRI, Riemannian Geometry, Retinotopic areas, hMT/V5+

\* Odyssee Lab., INRIA Sophia-Antipolis/ENPC/ENS, France

<sup>†</sup> Perception Lab., INRIA Rhône-Alpes, France

## **Connexions anatomiques du cortex visuel humain : validation et nouveaux aperçus basés sur l'algorithme GCM exploitant l'imagerie IRM-D.**

**Résumé :** Divers approches ont été proposées pour reconstruire les connexions de la matière blanche à partir d'Images de Tenseur de Diffusion (DTI). Dans cette étude, nous validons une technique de tractographie géométrique récemment introduite, l'algorithme GCM (Geodesic Connectivity Mapping), capable de s'affranchir des principales limitations dont pâtissent les approches de ce type. En particulier, l'algorithme CGM nous permet de caractériser avec succès les connexions anatomiques du cortex visuel humain de bas niveau. Nous retrouvons des résultats déjà observés concernant la topologie des radiations optiques reliant le LGN à V1 ainsi que l'organisation des fibres splénium par rapport à leur origine dans le cortex visuel. Enfin, notre étude apporte de nouveaux aperçus concernant les connexions du complexe MT humain (hMT+) et les aires rétinotopiques.

**Mots-clés :** IRM de Diffusion, Géométrie Riemannienne, aire rétinotopique, hMT/V5+

## 1 Introduction

Understanding the relationship between anatomical structure and function is a fundamental issue in neuroscience. In the last decades, neuroimaging advances have been providing ever more promising means to non-invasively address this fundamental issue, thus opening the possibility to investigate in vivo normal and patients cerebral architecture and activity. This is especially true for Magnetic Resonance Imaging (MRI), which allows to combine anatomical (structural MRI), functional (functional MRI) and white matter connectivity (diffusion MRI) information at a spatial resolution of a few millimeters.

High resolution anatomical images are routinely used to segment cerebral tissues and extract 3D models of different tissues including the cerebral cortex. Various approaches have been proposed to achieve these computations [12, 10, 58]. Since its discovery in the early 90's [46], Blood Oxygen Level Dependent (BOLD) fMRI has been increasingly used to identify and characterize functionally various cortical areas. This is specially the case in the visual cortex where retinotopic mapping and functional localization can successfully be used [25, 60, 55].

Diffusion Tensor Imaging (DTI) is the most widespread way to model diffusion MRI data: the probability density function of the three-dimensional water molecules motion, at each voxel of a DT image, is modeled as a local Gaussian process whose covariance matrix is given by the diffusion tensor [1]. Among other applications including the characterization of local tissue anisotropy [34], DTI can be used to estimate the anatomical connectivity across remote brain regions. Various approaches have been proposed to tackle this problem. They can be divided into three main classes: local, stochastic and geometric approaches.

Local approaches, based on line propagation techniques, rely on the fact that the eigenvector of the diffusion tensor associated with the major eigenvalue provides a relatively accurate estimate of the orientation of fiber bundles at each voxel. These methods may be refined to incorporate some natural constraints such as regularity or local uncertainty and to avoid being stopped in regions of low anisotropy [44, 33]. All these efforts aim to overcome the intrinsic ambiguity of diffusion tensor data arising from partial volume effects at locations of fiber merging, kissing or crossing. If they can provide relatively accurate models of the main white matter macroscopic bundles, these methods are sensitive to noise and partial volume effects and cannot give a quantitative measure to evaluate the degree of connectivity between brain locations.

Stochastic tractography algorithms were introduced by modeling the uncertainty of the local fiber orientation [2, 21]. Through uncertainty propagation, they provide a powerful means to evaluate the probability of connection between remote points of the white matter. However, the intrinsic drawback of these methods is their computational complexity since it is necessary to resort to Markov Chain Monte Carlo methods or to evaluate probability density functions at enough locations of the space of interest.

Geometric methods use either Level Set methods [45, 37, 31], Fast Marching methods [50] or iterative sweeping techniques [30] to evolve a front on the basis of the diffusion tensor directional information. Although more naturally able to exploit the whole tensor information in the connectivity estimation, these approaches are usually prone to interpolation errors at the boundary of the evolution domain, which may lead to erroneous connections in highly convoluted areas. Besides,

this class of methods suffers from a high computational complexity like the stochastic algorithms. Finally, most implementations work directly on the whole DT image, which can lead to anatomically impossible connections across non white matter tissue.

In this study, we validated a recently introduced geometric tractography technique, called Geodesic Connectivity Mapping (GCM), which overcomes the above mentioned limitations [52]. With the GCM technique, we could characterize anatomical connections in the human visual cortex, reproducing previous findings [15, 11, 4, 7, 6] and bringing further insights regarding their organization.

## 2 Methods

### MR data acquisition

3 healthy subjects with normal or corrected to normal vision participated in two separate scanning sessions, to acquire the functional and diffusion weighted images, respectively. In each session, a high resolution anatomical scan was acquired and later used as references to coregister the two sessions. All scans were acquired on a 3T Bruker MEDSPEC 30/80 Avance scanner with a birdcage head coil.

### *Structural MRI*

High resolution anatomical scans were acquired through a 15mns 3D-gradient echo sequence with inversion-recovery [TE 5ms; TR 25ms; IT 800ms; acq. matrix 256x192x104 reconstructed to 256x256x128; voxel size 1x0.75x1.22mm<sup>3</sup>].

### *fMRI*

During each functional scan, 151 Echo Planar Images were acquired over 5 mn 19 s using a coronal sequence [TE 35ms; TR 2111ms; Angle 70°]. Each functional image spans 20 coronal slices 3mm thick and 2x2mm<sup>2</sup> in plane resolution, approximately orthogonal to the calcarine sulcus covering the occipital retinotopic areas and extending anteriorly to confidently include hMT+ region [17]. The first five images were systematically discarded to avoid magnetic saturation effects. The 144 following images correspond to the visual stimulus per se. The last two images were taken to allow slice-timing correction preprocessing.

### *Diffusion Tensor Imaging*

In a pilot study, we first tried different acquisition parameters to obtain the best diffusion weighted images, having fixed TR=10000ms, TE=86ms, voxel size 2x2x2mm<sup>3</sup>. We finally used 12 diffusion directions for a single b value of 1000 s.mm<sup>-2</sup>, which is consistent with other studies [27] and allows to increase the number of repetitions for each gradient direction to achieve a better SNR. Each gradient directions was hence repeated 10 times. 8 standard T2 images (i.e. without diffusion sensitization or b=0 s.mm<sup>-2</sup>) were also acquired.

### Visual stimuli

Stimuli were generated under Matlab 6.1 using the Image Processing Toolbox (Matlab, The Mathworks), providing an avi file with eighteen 300x300 pixels frames per second and lasting 5mn04sec. Visual stimulation was synchronized with the acquisition through a trigger sent by the scanner at the beginning of each scan. Stimuli are displayed at 72Hz by a SONY video-projector, placed in a custom-designed Faraday cage inside the scanner room, onto a large adjustable mirror then onto a translucent screen inside the bore at the back of subjects head and finally reflected by a custom designed mirror placed at 5cm above subjects eyes. This setup leads to a display subtending a visual angle of 20.9°x20.9°. The stimuli are all presented within a circular aperture of 19.5° in diameter. During the first 5 and last 2 scans, a mid grey-level image with the 0.5° red fixation cross was shown to the subjects.

Phase-encoded stimulus for the retinotopic mapping consisted of a 9Hz flickering black-and-white checkerboard into a  $80^\circ$  rotating wedge; 8 complete rotations, either clockwise or counter-clockwise, were performed in each scan.

A classical block design paradigm was used to reveal the human mid-temporal complex, hMT+, supposed to comprise human homologues of at least macaque MT and MST [16, 29]; the stimulus was a black and white random dot pattern (maximum contrast) on a mid-grey background with a  $10.28 \text{ dots.deg}^{-2}$  density presented in 2 different conditions, each presented during blocks of 8 RT (16.888sec): static (STA), i.e. the same image for all the block duration and coherent (COH) when dots were moving at  $7.53 \text{ deg.sec}^{-1}$  radially in a 2Hz inward and outward alternation. Dots leaving the mask were replaced through a radial wrap-around constrained to keep the dots density constant.

### Image processing pipeline

Each dataset was analyzed on a subject basis to avoid undesirable effects such as the strong smoothing implied by standard normalization procedures. [62] showed it was possible to obtain geometrically matched fMRI and DWI with appropriate acquisition sequences, therefore avoiding various distortions correction steps. However, these images are not coregistered with the anatomical image and this procedure supposes to acquire data with the same volume prescriptions. In this study, since (i) we considered complementary information from 3 different MRI modalities (anatomical, functional and diffusion-weighted images), (ii) acquired two distinct sessions for each subject and (iii) used different slice prescriptions for the different modalities, a common or reference analysis space was required. We used the mean T2-weighted image, further corrected for EPI geometric distortions (see below), as reference space. We note *umean T2* this reference image. This choice minimized the deformations and interpolations of the diffusion-weighted images acquired within the same run using a similar sequence. Each type of image received specific processing detailed in the following paragraphs and the extracted useful information was finally coregistered to the *umean T2* reference image. Figure 1 summarizes the overall processing pipeline used in this study.

#### *Anatomical image.*

High resolution anatomical images acquired in both sessions allowed precise inter-session coregistration using SPM2 algorithm. We note *M1* the estimated transformation mapping anatomical image from session1 to anatomical image from session2. The latter was further coregistered with the *umean T2* reference image by transformation *M2*. Structural information was processed from both anatomical scans to segment grey and white matter tissues and build a 3D model of the cortical surface using a combination of the BRAINVISA<sup>1</sup> package and local methods [18].

#### *Visual areas functional definition.*

Statistical Parametric Mapping (SPM2; [www.fil.ion.ucl.ac.uk/spm/](http://www.fil.ion.ucl.ac.uk/spm/)) was used to analyze functional data for the retinotopic and hMT+ mapping. Images were first realigned with the INRIAalign software [20] and coregistered with the anatomical image with SPM2, then smoothed through an appropriate cortical surface based smoothing method described elsewhere [63], with a 3mm equivalent Gaussian filter FWHM. Temporal high-pass and low-pass filtering were also performed on the time-courses

<sup>1</sup><http://brainvisa.info/index.html>

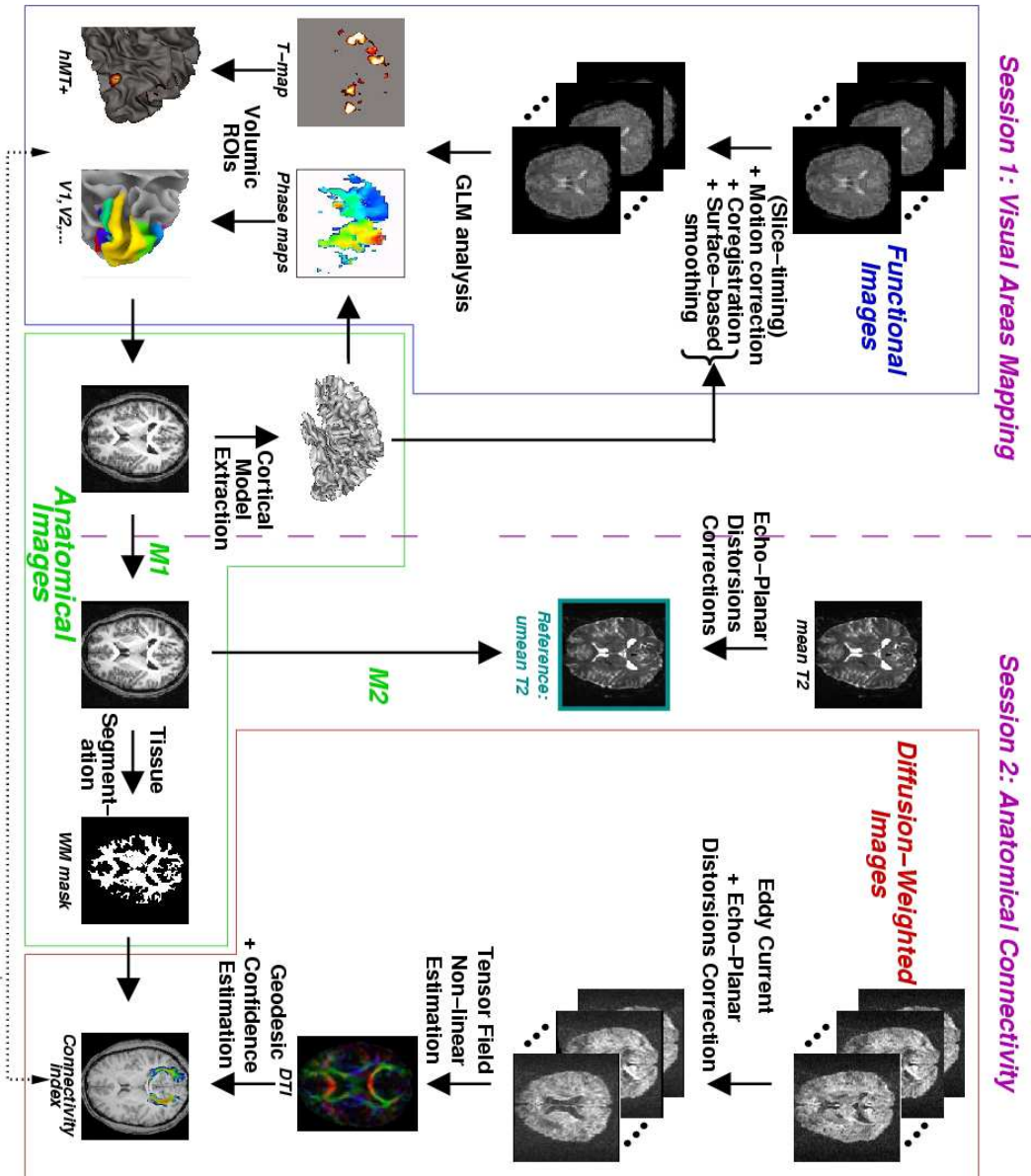


Figure 1: The image processing pipeline. Functional, diffusion-weighted and anatomical images receive specific processing and are realigned on a reference image, *umean T2*, for the connectivity maps computation (see text for details).

to respectively remove low-frequency signal drifts and high frequency noise. Retinotopic mapping and hMT+ localizer data were then analyzed separately with respective general linear models [22]. Retinotopic stimuli were modeled by cosine and sine functions at the stimulus frequency and a voxelwise F-test thresholded at  $P < 0.001$  was used to identify responding voxels. The local signal phase, related to the stimulus position, was then given by the arctangent of the ratio of the parameter estimates for both regressors [64].

Each condition of the hMT+ localizer stimulus was modeled by a classical boxcar function convoluted with a canonical hemodynamic response function model. A T-contrast was computed to compare COH and STA conditions and thresholded at  $P < 0.001$ . We considered as hMT+ the activated cluster within or close to the inferior temporal sulcus [61, 17].

Subsets of connected voxels were extracted for each area and further used as ROIs in the connectivity analysis. Since diffusion anisotropy is relatively low in grey matter voxels [51], such as in the visual cortex [62], we defined white matter ROIs, considering the white matter voxels closest to the cortical ROIs. Specifically, volumic ROIs were automatically computed from their identification on the GM/WM interface by projecting the respective surface-based labels along the surface normal inside the white matter voxels. Each ROI voxels subset was then coregistered to the *umean T2* reference image by the transformation  $M1 \circ M2$  and further masked to solely lie within the white-matter mask extracted from the high resolution anatomical image. Possible intersections between each pair of white matter ROIs were automatically removed from the analysis.

#### *Diffusion-weighted images (DWI).*

*T2 image:* the 8 T2-weighted images were motion corrected using the INRIAAlign software before being averaged. The resulting mean T2 image was then processed to correct geometric EPI distortions caused by magnetic susceptibility inhomogeneities, i.e. magnetic field inhomogeneities particularly found at the interfaces between different tissues [32]. Based on the phase map acquired during the DWI data recording session, which maps the spatial distribution of field inhomogeneities, we used the SPM interfaced toolbox “Fieldmap” ([www.fil.ion.ucl.ac.uk/spm/toolbox/fieldmap](http://www.fil.ion.ucl.ac.uk/spm/toolbox/fieldmap)) to compute and apply a voxel displacement map accounting for these susceptibility artifacts. As mentioned above, the resulting *umean T2* image served as reference image for connectivity maps computation.

*DTI:* DWI data were first preprocessed to minimize the distortions induced by eddy-currents and related to the large diffusion-sensitizing gradients [42]. We then applied to the resulting images the EPI geometric distortions correction algorithm used for the mean T2 image. The diffusion tensor image (DTI), a field of 3x3 real symmetric positive-definite tensors along the image domain, was finally computed with a non-linear robust gradient method proposed in [38] which naturally yields symmetric and positive definite solutions for  $D$ . We have observed particularly significant differences with the classical least square method in highly anisotropic regions such as the corpus callosum, where the latter method could lead to non-positive tensors.

#### **Seed voxels placement**

A crucial aspect for any fiber tracking method is the location of the initial seed. The seeds for the GCM algorithm were selected depending on the considered tracts.

#### *LGN seed voxels identification*

Lacking a precise functional localization of the LGN, we first identified LGN seeds voxels with a classical streamline technique. To do so, we manually selected in each hemisphere a rough thalamus sub-region which obviously included the expected LGN location. More specifically, based on both anatomical and diffusion tensor image prior information, the initial region was identified anterior to the lateral ventricles and only voxels with a relatively high anisotropy ( $FA \geq 0.15$ ) were kept. Diffusion tracts starting from each selected voxel were estimated with a classical streamline tractography technique [33] and further automatically filtered to keep the fibers heading to the ipsilateral retinotopically identified area V1. Only fibers reaching a 3 voxels wide band around the functionally defined V1 region were kept. This approach is very similar to that of Conturo and colleagues [11], although we did not oversample the DTI data, thus getting less fibers than in the latter work. The starting voxels of the remaining fibers were finally labeled as the LGN voxels. We typically found a region of 5 connected voxels in each hemisphere, consistent with the reported LGN size both in previous anatomical [28] and fMRI studies [5]. Beyond yielding an anatomical connectivity based delineation of the LGN, the reproduction of the well-known visual pathway as well as the likely extent and location of the LGN ROIs validates our diffusion-weighted images quality as well as our image processing pipeline.

#### *Splenium seed voxels*

Seed voxels in the splenium were manually traced on a mid-sagittal slice of the anatomical image as the most posterior and ventral portion of the corpus callosum. The voxels subset was further masked by the white matter tissue mask.

#### *Other tracts*

For connectivity mapping starting from the functionally identified visual areas, we simply used the white-matter ROIs defined with the procedure detailed above.

### **Connectivity maps and fiber tracts computation**

#### *Streamline technique*

To date, streamline techniques are very often used since their implementation is quite straightforward and the basic idea underlying the algorithm is intuitive: at each voxel, the eigenvector associated to the largest eigenvalue is supposed to reflect the microstructure of the underlying tissue and parallels the mean fiber orientation in that voxel. Hence, the major eigenvector field is treated as a flow field and integrated in order to estimate streamlines, expected to coincide with white matter fibers. In the implementation we used, the integration is typically performed numerically with subvoxel precision through a 4<sup>th</sup> order Runge-Kutta scheme [39].

#### *Geodesic Connectivity Mapping (GCM) Technique*

#### *The Riemannian geometry framework applied to DTI*

We used an approach based on a Riemannian geometric framework to compute (i) a distance function to a given point of interest (or *seed point*)  $x_0$ , (ii) the putative fiber path linking any voxel of a given brain region  $V$  to  $x_0$  and (iii) a connectivity map, i.e. a confidence measure associated with each fiber. We refer to this technique as Geodesic Connectivity Mapping (GCM). In this geometrical formulation of DTI connectivity mapping, the DTI is modeled as a Riemannian manifold  $M$  whose metric is directly related to the diffusion tensor  $D$  modeling the local diffusion properties of water molecules. As shown in [36, 45], the metric  $G$  of  $M$  is given by  $G = D^{-1}$ . From this metric, a distance function  $u(x_0, x)$  between a given seed point  $x_0$  and any other location  $x \in V$  of the brain mask can be evaluated. The solution  $u$  at any voxel  $x \in V$  can be interpreted as the minimum arrival time  $t \geq 0$  to reach  $x$  starting from  $x_0$  on the manifold  $M$ . It is obtained by solving the anisotropic Eikonal equation:

$$\|\nabla u(x)\|_G = 1 \quad (1)$$

where  $\nabla u$  denotes the gradient of  $u$  on the manifold  $M$  and  $\|\cdot\|_G$  is the norm associated to the metric  $G$ . Considering the low anisotropy in the grey matter tissue, we consider for  $V$  the set of white matter voxels obtained from a segmentation of the anatomical image (see methods).

The geodesics of  $M$  are considered as putative white matter bundles linking any voxel  $x \in V$  to  $x_0$ . As such, a geodesic connecting any voxel  $x \in V$  to the seed voxel  $x_0$  always exists. If an actual white matter fiber connects  $x$  and  $x_0$ , the associated geodesic coincides with the fiber. However, for any  $x \in V$ , the associated geodesic does not necessarily coincide with an *actual* white matter fiber. It is indeed highly unlikely from an anatomical point of view that a given brain locus could be directly connected to *every* other brain locations. To overcome this issue, a connectivity measure can be estimated for each geodesic curve. This enables us to discriminate likely and unlikely white matter connections. In this study, we considered, for each estimated geodesic, statistics along the curve of the following local confidence measure:

$$C(x) = \|f^*(x)\|_E$$

where  $\|\cdot\|_E$  is the Euclidean norm.  $f^*(x)$  corresponds to the so-called optimal dynamics at voxel  $x$ . It can be interpreted as the tangent to the geodesic at location  $x$ . In other words, it coincides with the optimal direction to follow in order to minimize the distance between  $x$  and  $x_0$ , and recover the optimal path. Moreover, it can be shown that  $f^* = -\nabla u$ . We claim that  $C$  is a natural local measure of connectivity since it can be thought of as the local velocity of the underlying diffusion of water molecules in the white matter tissue. From this local connectivity index, we compute its first and second order statistics along the geodesic:

$$\mu(x) = \mathbb{E}[C(x)] \quad \text{and} \quad \sigma(x) = \sqrt{\mathbb{E}[C(x)^2] - \mathbb{E}[C(x)]^2}$$

An ideal fiber linking  $x$  to  $x_0$  will typically have a large mean value  $\mu(x)$  and a small standard deviation  $\sigma(x)$ . This connectivity measure provides a means to distinguish likely and unlikely fibers. Since each voxel  $x \in V$  can be assigned a geodesic reaching  $x_0$ , we have a pair  $(\mu(x), \sigma(x))$  at each voxel. In the remainder, we call  $\mu$ -map and  $\sigma$ -map the respective images of  $\mu$  and  $\sigma$  values.

### Numerical methods

Regarding the numerical computation of distance functions, geodesics and connectivity measures, we used two different approaches respectively based on the level set framework [37] and a control theory formulation [52]. If both interpretations are mathematically equivalent, they focus on different aspects of the problem. In the level set (or dynamic) approach, the emphasis is on the description of the manifold geometry, while in the Fast Marching point of view (or static) approach, the emphasis is on the optimal dynamics  $f^*$ , which coincides with the intrinsic gradient of the distance function.

We give below an overview of both methods.

#### *The Level Set Approach.*

We first used the level set method described in [36, 37]. As shown e.g. in [47, 53], equation (1) can be reformulated in the level set perspective. This is achieved by introducing a new function  $\psi$  such that the evolving function  $u_t$  is a level set of  $\psi$ :

$$u_t = \{x \in V : u(x) = t\} = \{x \in V : \psi(x, t) = 0\}$$

Then, it can be shown [47] that finding  $u$  satisfying equation (1) is equivalent to solving the Partial Differential Equation (PDE):

$$\begin{cases} \frac{\partial \psi}{\partial t} + \|\nabla \psi\|_G = 0 & \forall t > 0 \\ \psi(x, 0) = \psi_0(x) \end{cases} \quad (2)$$

where  $\|\nabla \psi\|_G = \sqrt{D\psi^\top G^{-1}D\psi}$ .

Finding the distance function  $u$  boils down to evolving  $\psi$  while tracking, for all  $x$ , the time  $t^*$  when  $\psi$  changes sign. In this approach, the distance function  $u(x_0, x) \forall x \in V$  to a given seed voxel  $x_0$  is estimated by evolving a front in the manifold  $M$ . Starting from  $x_0$ , the speed at which the front propagates is directly related to the local diffusion tensor  $D$ . The larger the local tensor eigenvalues are, the faster the local front propagation will be in the associated eigenvectors directions. Hence, evolution is fastest along white matter paths. The front arrival time at each voxel generates the distance function to  $x_0$ . Geodesics are then obtained by back-propagating along the function  $u$  gradient field from any voxel  $x \in V$  towards the origin  $x_0$ . The related connectivity measures  $\mu(x)$  and  $\sigma(x)$  are finally estimated during the computation of this optimal pathway linking  $x$  to  $x_0$ , by integration of the local criterion  $C$  along the entire geodesic.

#### *The Fast Marching Approach.*

Facing two major limitations of the level set approach, namely the high algorithmic complexity leading to long computational times and, more importantly, numerical difficulties to properly deal with the white matter mask boundaries, we used a recently proposed formulation of the problem. By recasting problem (1) into the control theory framework and numerically solving it with a Fast Marching Method (FMM), the authors achieved a dramatic computational improvement to evaluate the quantities of interest. The theoretical issues, as well as the C++ implementation, were developed in a collaboration between the Odyssee laboratory and the UCLA vision Laboratory. We refer the reader to [52] for an in-depth study of the approach and its contributions.

Briefly, in this formulation, the problem comes down to estimating the optimal vector field  $f^*$  (optimal dynamics) corresponding to the field of the geodesics velocity in  $M$  (which also coincides with  $-\nabla u$ ). This is achieved using a Fast Marching based algorithm. Starting the front from an initial seed position  $x_0$ , the Fast Marching Method (FMM) systematically marches the front outwards one grid point at a time, by always choosing the optimal grid points configuration (the so-called optimal simplex) yielding the smallest update value of the distance function  $u$ . This is the well-known principle of causality. FMM thus builds the optimal dynamics  $f^*$  by propagating the information “one way”, requiring a single pass over the domain  $V$ . The distance function  $u$  is now a byproduct of the algorithm, no longer necessary for subsequent computations. Besides, the connectivity maps  $\mu$  and  $\sigma$  are computed “on the fly”. Indeed, based on the optimal simplex, one only needs to compute the local value for  $C(x)$  and  $C(x)^2$  and then build on previous values to derive  $\mu$  and  $\sigma$  associated to the geodesic linking  $x_0$  to the current voxel. If needed for visualization purposes for instance, the geodesic paths can be straightforwardly reconstructed by following the optimal dynamics  $f^*$ .

This method allows the use of Fast Marching (FM) algorithms, yielding a tractography approach that offers many advantages over existing work, including the level set method we first used:

- the method is efficient since it computes simultaneously the optimal dynamics and the statistics of our local connectivity measure; besides, the explicit computation of the geodesics is not mandatory to get the connectivity measure maps,
- the computation time is dramatically improved, from 20 minutes to get the distance function with the level set formulation to 7 seconds with the FM algorithm,
- the method naturally handles the constrained computation within highly convoluted regions such as in the occipital cortex white matter (see figure 2),
- the algorithm exhibits a higher robustness with respect to noise over the level set implementation, as validated by numerical experiments on synthetic datasets; this robustness is in particular due to the strategic and consistent choice of the simplex used for the approximation of the gradient, the distance function and of the statistics of the connectivity measure.

The results presented below were systematically obtained with the Fast Marching based algorithm. Notice however that the level set method led to qualitatively similar results, although the computation time was by far higher and the numerical issues mentioned above could lead to anatomically impossible front propagation (figure 2), requiring iterative manual modifications of the white matter mask.

#### *Connectivity indices computation*

We used the following methods to compute connectivity within the splenium region and to estimate hMT+ connectivity with retinotopic areas.

To study splenium tracts, we analyzed connectivity maps in the splenium voxels, starting from our retinotopically (or functionally for hMT+) defined ROIs. Each ROI was considered separately. We note  $X = (x_i)_{i=1,\dots,n}$  a specific  $n$  voxels seed ROI (e.g. left hemisphere V1) and  $Y = (y_j)_{j=1,\dots,m}$  the  $m$  splenium voxels identified on a mid-sagittal slice. For each seed voxel  $x_i$ , the corresponding  $\mu$ -map and  $\sigma$ -map were computed with the GCM method. We therefore have the mean and sigma values for each optimal path  $\gamma_{i,j}$  linking  $x_i$  to  $y_j$ . We then filter these maps to remove the highest

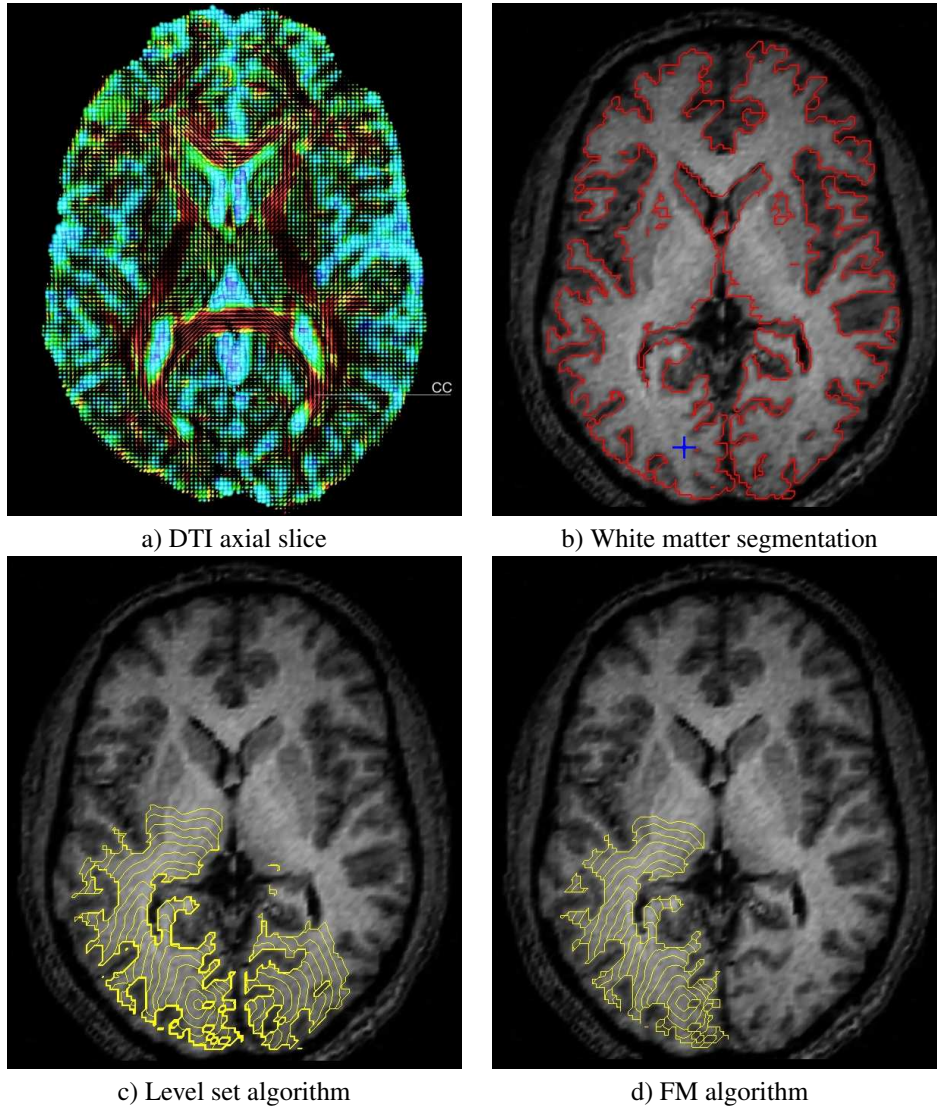


Figure 2: Distance function computed from DTI data (a) to an occipital seed voxel, the blue cross in (b) in a white matter mask (red line in (b)). Yellow lines depict distance function isovalues in the range  $[0;1500]$ , computed through the level set (c) or the Fast Marching (d) algorithms. Front diffusion of the level set method does not necessarily respect the white matter mask topology, leading to anatomically impossible connections through CSF voxels (c). This numerical problem is avoided in the Fast Marching method which naturally respects the mask topology (d).

variance paths and compute a single mean  $\mu$ -map in the splenium. Specifically, for each splenium voxel  $y_{j_0}$ , we have  $n$  putative paths  $\gamma_{i,j_0}$ . We discard a given proportion  $p$  of these  $n$  connectivity paths, removing paths with highest variance  $\sigma$ . The mean connectivity indices of the remaining putative fibers are then averaged, leading to a single mean value  $\mu$  at voxel  $y_{j_0}$ . The procedure is repeated for each  $y_j, j = 1, \dots, m$ . The resulting  $\mu$  map is interpreted as the mean connectivity between area  $X$  and the splenium.  $p$  was arbitrarily set to 10%, but the qualitative results did not differ for  $5\% \leq p \leq 20\%$ .

Regarding hMT+ connectivity with retinotopic areas, the connectivity indices were computed as follows. Taking as seeds each hMT+ voxel  $(x_i)_{i=1,\dots,n}$ , we compute the  $\mu$  and  $\sigma$  maps with the GCM method. For each  $x_i$ , we then discard a given proportion  $p$  of paths with highest  $\sigma$  values among the  $m$  paths linking target ROI voxels  $(y_j)_{j=1,\dots,m}$  to  $x_i$ . The mean  $\mu$  value of the remaining paths is then computed and assigned to voxel  $x_i$ . At each hMT+ voxel, we end up with a mean connectivity value for each retinotopically defined target ROI. Similarly to splenium fibers,  $p$  was arbitrarily set to 10%, but the qualitative results did not differ for  $5\% \leq p \leq 20\%$ .

### 3 Results

We first validated our protocol and connectivity mapping technique on the previously characterized optic radiation tracts before investigating callosal connectivity and intra-cortical connectivity across the functionally identified visual areas.

#### Optic radiations

Since the optic radiations were often reconstructed in diffusion tractography studies [11, 4, 6, 7], we decided to start the validation of our fiber tracking approach by considering this well characterized fiber bundle, which links the Lateral Geniculate Nucleus (LGN) to area V1 in the occipital cortex. Starting from each previously identified LGN voxels (see methods), we computed the connectivity index maps with the GCM method. As we were not concerned here with inter-hemispheric connections, the GCM computation was restricted to the ipsi-lateral hemisphere of the seed voxel. To compare our method with a standard approach, we also reconstructed the fibers leaving the LGN with a classical streamline technique. Figure 3 shows one  $\mu$ -map per hemisphere in two subjects. As each map is restricted to its respective hemisphere, we merged them in a single image and overlaid the result on an axial slice of subjects' anatomical image. The seed voxel of each  $\mu$ -map is shown in black. The highest connectivity index values (dark red) are systematically found within the typical path of the optic radiations. Besides, highest values were found in the retinotopically identified V1 region. These results were found for each LGN seed voxel in the 6 hemispheres we analyzed. Consequently, for each connectivity maps, the voxel with maximum connectivity mapping index (which lay in area V1) was identified and the geodesic linking that voxel and the seed point was traced. Figure 4 shows the reconstructed fiber bundles obtained with the streamline technique (blue) and the GCM technique (red). Although the thalamo-occipital fibers estimated with streamline and geodesic methods qualitatively match and are consistent with known anatomy, we noted some differences between reconstructed tracts.

Most fibers estimated by streamline propagation fail to reach the V1 white matter ROI, unexpect-

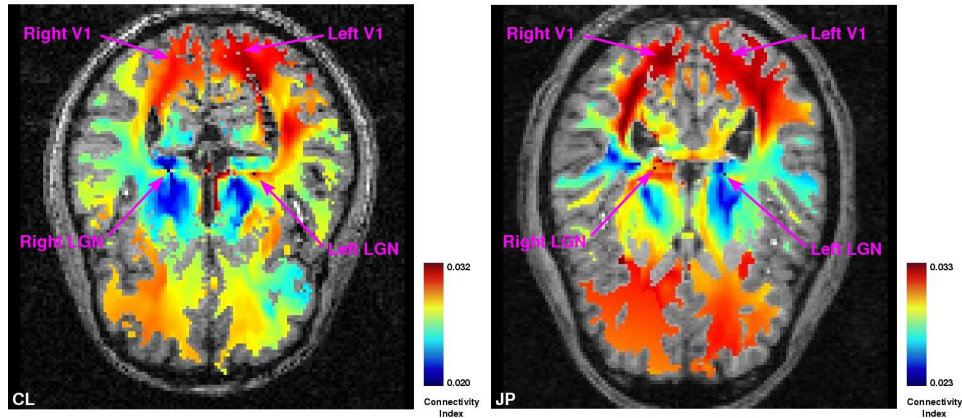


Figure 3: Connectivity  $\mu$ -maps obtained in two subjects estimated separately from one LGN seed voxel (in black) for each hemisphere. The highest connectivity index values are found along the putative optic radiations paths, with the maximum value within area V1.

edly heading in a ventral direction a few millimeters before reaching the V1 region. We attribute this unexpected trajectory ending to an improbable connection with another fiber bundle crossing the thalamo-occipital track. This observation led us to use a relaxed constraint to filter the fibers passing closely to V1, as mentioned in the above description of the LGN seed voxel identification procedure (see methods). Note that [11] also used a 1cm band within the white matter, laterally located to the activated occipital cortex to filter their thalamo-occipital fibers (see [11], figure 3). Besides, other DTI tractography works showing this bundle do not exhibit an actual connection with a accurately defined V1 ROI, letting open the question of the fibers termination location.

On the other hand, GCM estimated tracts systematically reach our white matter V1 region, which illustrates an important advantage of the geometric front propagation method over local approaches. However, GCM fibers tend to converge rapidly after leaving the seed voxels, which denotes the less local characteristic of the method (see discussion).

### Callosal connections

For each hemisphere, the low-level visual areas represent and analyze only one half of the visual field, i.e. their respective contralateral hemifield. Nonetheless, homologue areas of both sides, such as left and right V1, have been shown to be connected, at least for the vertical meridian representations, through the splenium, a portion of the corpus callosum [9]. Following [15], we studied the GCM estimated connectivity maps of our functionally defined areas. We were interested in testing the capability of our GCM method to replicate the broad connection topology that Dougherty and colleagues reported in the region of the splenium.

Figure 5 shows the resulting mean  $\mu$ -maps for visual areas hMT+, V1, V3A and V4 respectively taken as starting ROIs in a mid-sagittal section of the brain for each subject. We do not represent

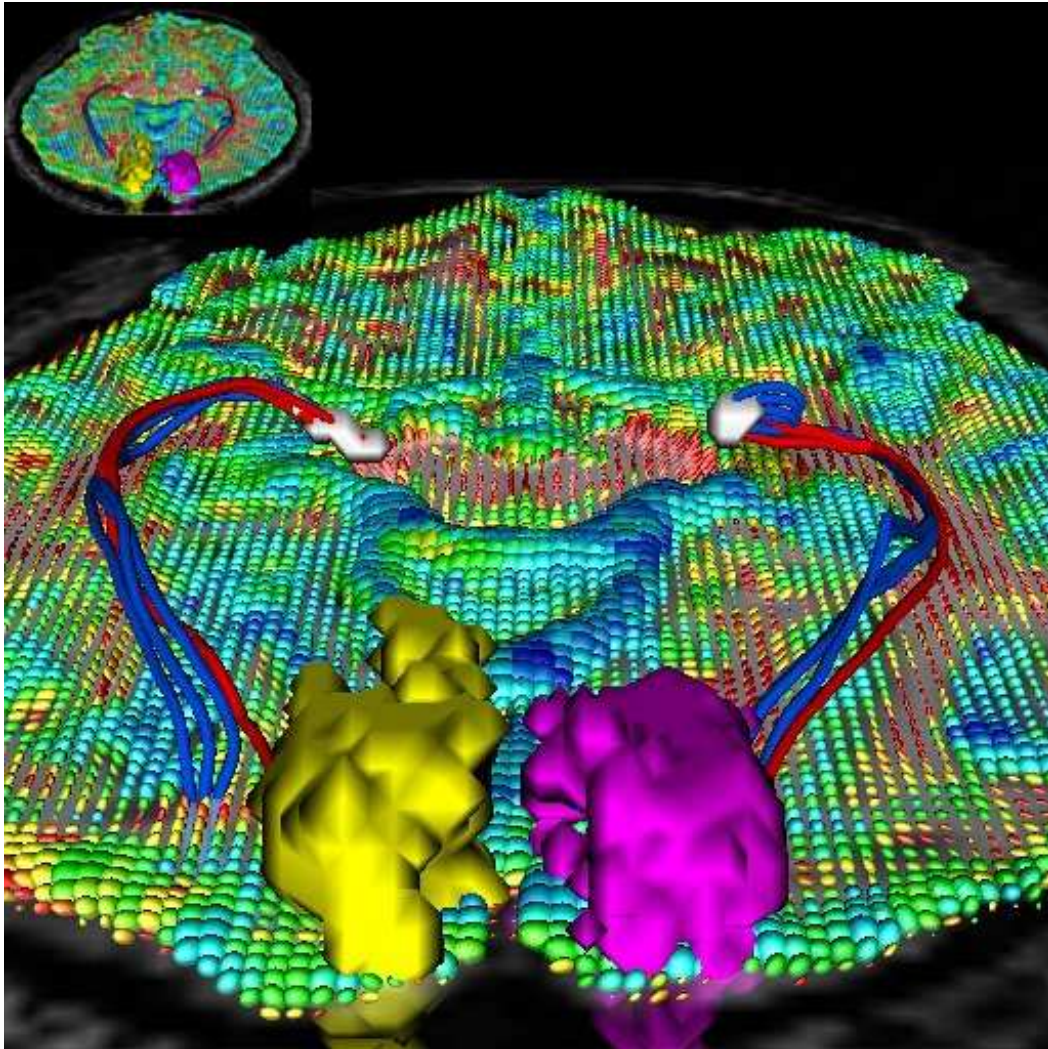


Figure 4: Optic radiation tracts estimated with a classical streamline method (blue) and with our GCM technique (red). The LGN seeds voxels (green), Left V1 (yellow), right V1 (purple) and an axial slice of the DTI are also represented. Tracts obtained with the streamline method can fail to reach area V1, as in the left hemisphere here. On the other hand, tracts estimated with our GCM technique systematically reach area V1, but they rapidly converge into a single bundle, illustrating the more global behavior of the method.

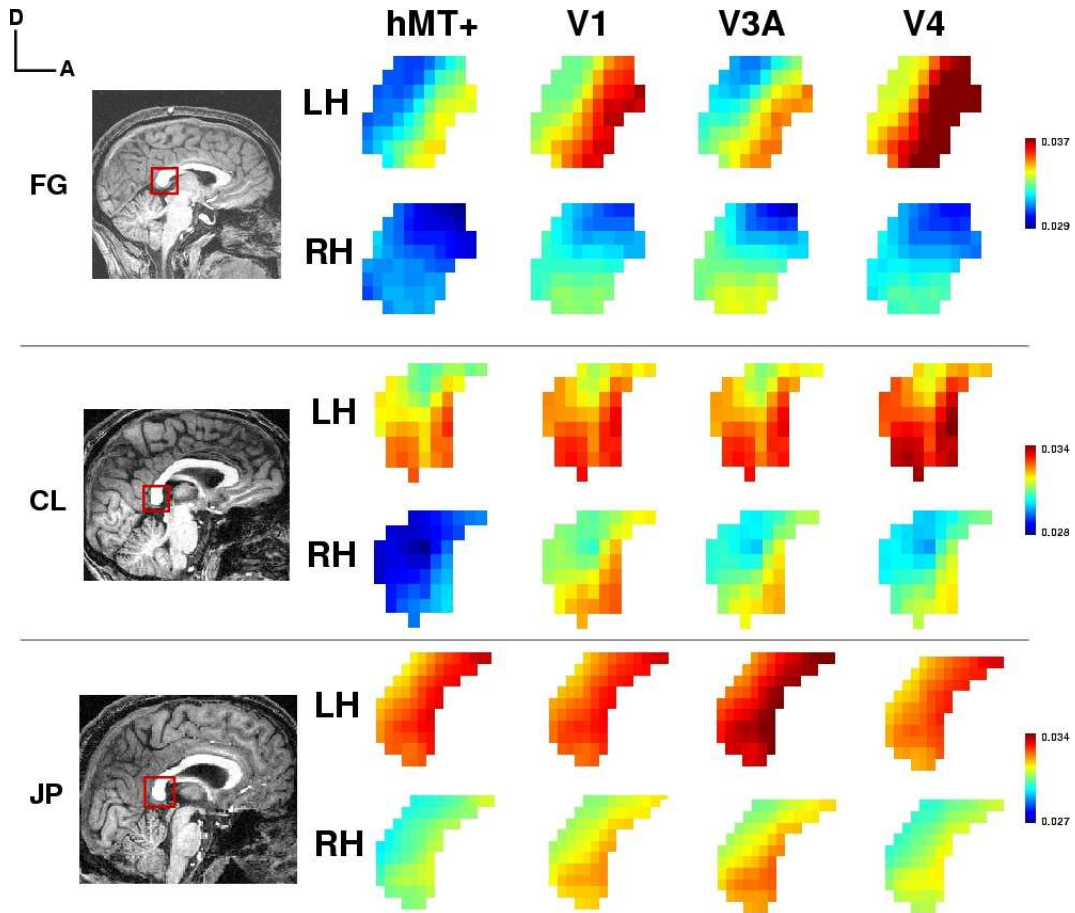


Figure 5: Mean connectivity indices from distinct visual areas to the splenium voxels. The mean connectivity values show a smooth gradient from postero/dorsal to antero/ventral splenium portions. Lowest connectivity values in the splenium are systematically found for hMT+.

here the mean  $\mu$ -maps for areas V2v, V2d, V3v and V3d, as they do not significantly differ from their closest neighboring areas on the cortical surface, i.e. V1v, V1d, V4 and V3A respectively (see discussion below).

Connectivity values are ordered similarly for each areas, with a smooth gradient from lowest values in the postero/dorsal portion of the splenium to highest values in its antero/ventral portion. Comparing the different origin areas, lowest connectivity values in the splenium were systematically found for hMT+. Regarding areas V1, V3A and V4, values are not consistent enough across subjects to in-

for a systematic topology in the occipito-callosal connections. However, V3A connectivity is higher than for V4 in 4 out of 6 hemispheres, suggesting a stronger callosal connectivity for dorsal with respect to ventral areas. Finally, we observed a systematic asymmetry between the maps associated to each hemisphere. The highest values were found for putative connections originating from the left hemisphere.

Figure 6 represents the most probable fibers linking each hMT+ voxel from both hemispheres to the

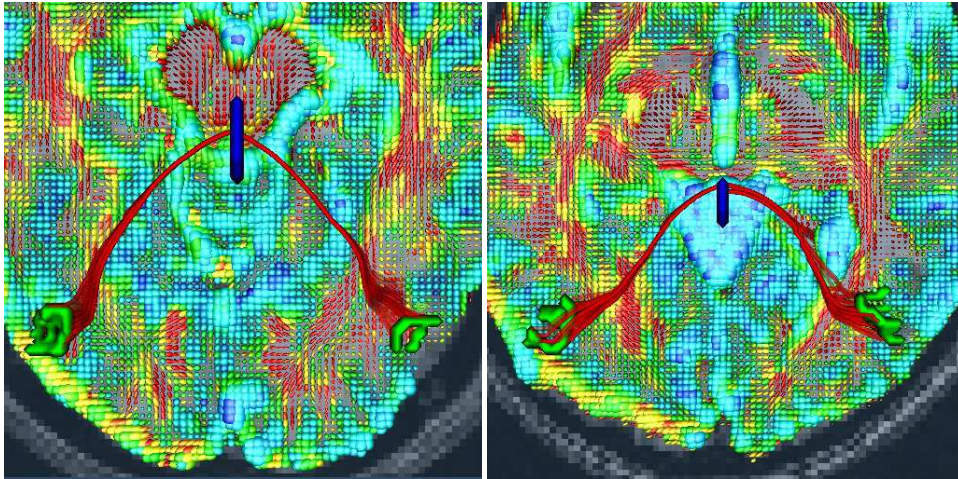


Figure 6: Independently estimated most probable fibers linking left and right hMT+ (in green) to the splenium (in blue) from two subjects (left CL and right JP).

splenium. We employed a similar method to that used to obtain the optic radiations fibers. More specifically, for each hMT+ voxel considered as a seed, we computed the related connectivity index maps. We then identified the splenium voxel with highest connectivity index and constructed the related geodesic. The estimated fiber tracts from the two hemispheres show a great spatial agreement.

#### **hMT+ intra-hemispheric connectivity**

Using a similar approach, we finally studied GCM of the human MT complex with the ipsilateral occipital retinotopic areas. Figure 7 shows a box plot of the mean connectivity values distribution for the different seed voxels of hMT+ across retinotopic areas. The boxes edges depict the values of the first quartile, the median and the third quartile. Values outside this box are also shown, to completely represent the distribution dispersion.

V1 and V2 systematically showed the highest connectivity values, suggesting highly probable connections with hMT+. V1 and V2 can hardly be distinguished, which can be attributed to their very close anatomical locations given our voxel size (see discussion). On the other hand, V4 systematically showed the lowest connectivity values, suggesting a weak direct anatomical connection with hMT+. It is more difficult to clearly distinguish the remaining areas V3v, V3d and V3A.

Similarly to the splenium data analysis, we clearly found higher connectivity values for the left

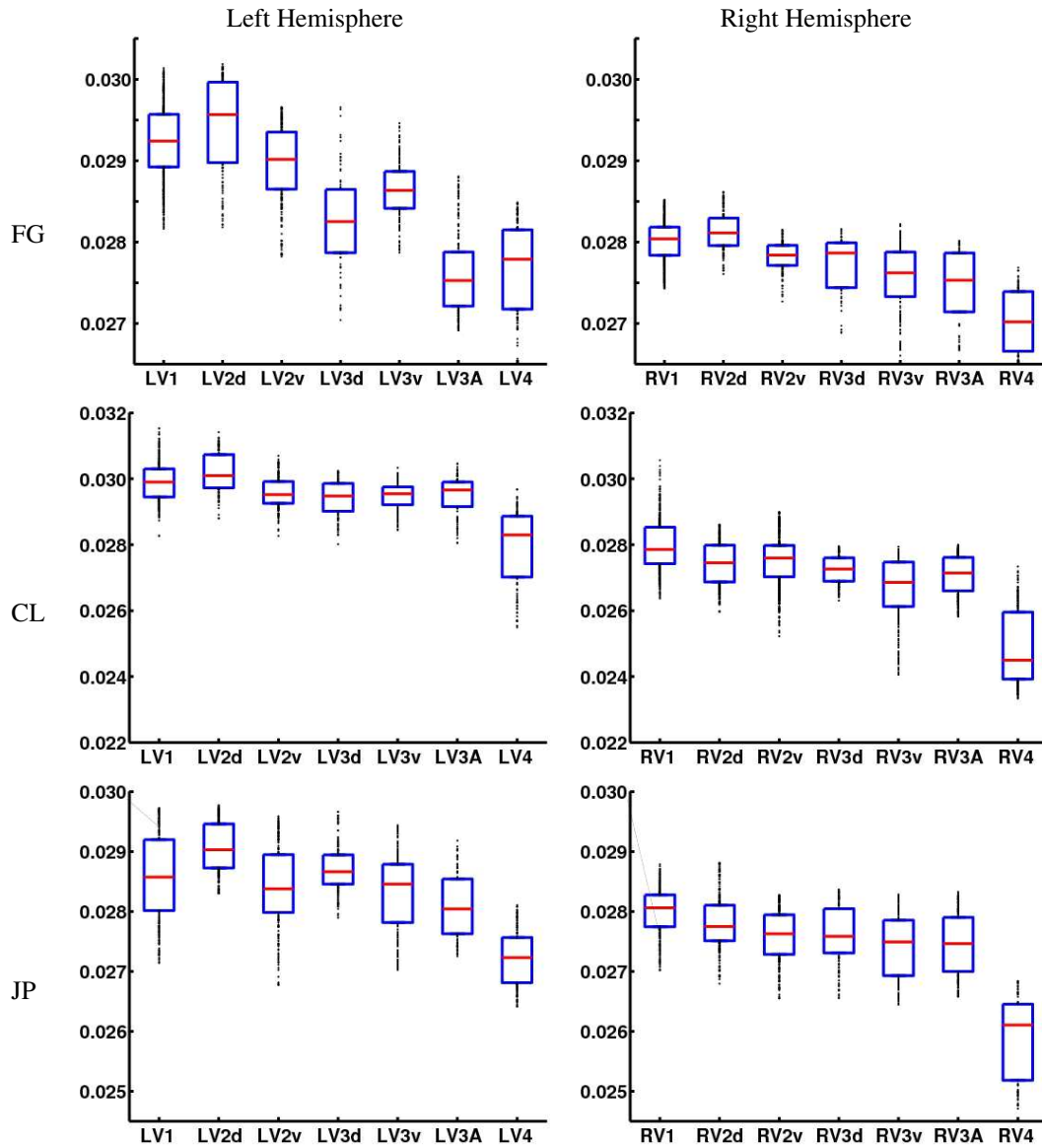


Figure 7: Mean connectivity between hMT+ and the retinotopic areas. V1 systematically shows highest values while V4 exhibits lowest values. Note also lowest values found in the right hemisphere compared to the left in the 3 subjects.

hemisphere as compared to the right, regardless of the area considered (see the values range on the vertical axes).

## 4 Discussion

We could successfully characterize connectivity along projection, callosal and association tracts in the human visual system with our GCM approach. Although our analysis is restricted to 3 subjects, we could successfully reproduce known results about the white matter tissue organization in this region of the brain. This validates our method. We shall first discuss methodological issues regarding DTI based tractography, with a particular emphasis on our GCM technique, before we address the results regarding current knowledge on the human visual brain connectivity.

### Methodological issues

#### *DTI Geodesic Connectivity Mapping: validity and limitations*

The current study provides a validation of the GCM approach to estimate DTI based connectivity mapping in the visual system. With its other application to the human motor system [35], this Riemannian geometrical approach, using the full tensor information, appears very useful to study anatomical connectivity in various cognitive systems. Geometrical tractography methods, such as the current GCM used in our study, have three main advantages over other tractography approaches. First they provide a connectivity measure between any pair of points within the white matter. This information can be used to build connectivity matrices over the whole brain or to rank putative connections pathways in the white matter. Then, geometrical approaches can deal with locally isotropic tensors occurring at fibers kissing or crossing. This is not the case with deterministic or probabilistic approaches where a FA threshold condition is often necessary to avoid unreliable fibers. Finally, these methods are less sensitive to acquisition noise, since they take advantage of the complete tensor information and of the less local behavior of the algorithm by comparison with streamline or stochastic approaches.

Although previous implementations turned out to be computationally intensive [36], the recently developed FM method allows a very fast estimation of connectivity maps and geodesic path construction, as well as an improved robustness to noise. Besides, this approach naturally deals with the convoluted geometry of the white matter mask, avoiding anatomically impossible tracts passing through CSF voxels (figure 2). We refer the interested reader to [52] for further details regarding the Fast Marching implementation.

There are however limitations both due to DTI by itself and to the geometrical connectivity mapping framework. First and foremost, the relatively poor spatial resolution of DTI (typically a few  $\text{mm}^3$ ) when compared to actual white matter fibers diameter (between 0.2 and 20  $\mu\text{m}$ ) has important implications:

(i) Only white matter “highways” may be properly recovered, which hardly represent every cortico-cortical connections; false negative connections are thus unavoidable and a precise discrimination between spatially close regions is still difficult to obtain. Our results on the visual system illustrate these spatial limitations. As mentioned above, we could hardly distinguish mean connectivity

maps for areas V1 and V2. Although surprising at first sight, this result can actually find a simple explanation when considering together the anatomical layout of these areas and the current spatial resolution of DTI. Areas V1d and V2d (and similarly V1v and V2v) respectively lie on the opposite banks of the same gyrus<sup>2</sup>. The white matter tissue separating the latter is therefore relatively thin, especially with 2mm isotropic voxels. Thus we cannot expect to easily distinguish the connectivity maps obtained with two opposite voxels in this gyrus. Improvement of the spatial resolution appears as the only way to solve this problem. Although still to be considered for the areas couples V3d/V3A dorsally and V3v/V4 ventrally, this gyral proximity is less pronounced since these areas borders appear less constrained by the sulco-gyral pattern than for V1 and V2 borders. Improvements in image acquisition protocols, such as parallel imaging, may overcome this spatial limitation, but a precise physical lower bound is still to be estimated.

(ii) The tensor model cannot handle properly fibers crossings or kissings that may occur within a voxel. Emerging approaches using higher order models based on High Angular Resolution Diffusion Imaging (HARDI) [19, 54, 48, 3, 13, 14] may provide an answer to this issue.

An intrinsic problem of the geometrical connectivity mapping approach used here comes from the absence of absolute threshold to confidently estimate fiber tracts from the connectivity maps [49]. Depending on the threshold choice (the  $p$  proportion), false positive or false negative connections may arise. Combination of complementary connectivity indices associated with each geodesics may prove to minimize this limitation. Furthermore, most tractography methods to date, including ours, are not symmetrical in the sense that putative paths reaching a position  $y$  while starting from  $x$  may not necessarily coincide with those linking  $x$  when starting from  $y$ . Besides, tracking within GM, although theoretically possible with geometrical approaches like the one we employed, still leads to difficult interpretations of the reconstructed connectivity maps and related tracts as the diffusion signal is poor in the cortical tissue. Last but not least, a direct validation of DTI based methods is still missing. Although reconstructed tracts such as the optic radiations in the current study or the motor pathway found in [35] are consistent with known anatomy, a quantitative validation could indicate the advantages and weaknesses of DTI based tractography methods. Ultimately, an animal study comparing the different tractography approaches with invasively identified connections would be of great interest to demonstrate their respective advantages and current DTI based tractography limits.

#### *Combined fMRI and DTI*

The fMRI areas identification confidently restrained our analysis into known brain regions. We thus avoided possible operator-dependent bias in seed placement or rough anatomically based inference. No obvious false-positive connections were found in our study.

---

<sup>2</sup>Note that Van Essen proposed an interesting mechanical tension-based theory to explain this particular folding pattern [57].

## Visual cortex connectivity

### *Thalamo-occipital fibers*

We first reproduced tracking of the thalamo-occipital fibers bundle connecting the LGN and V1. This fiber bundle was identified in various DTI tractography work, either with a deterministic streamline [11, 4] or a Fast Marching Tractography [7, 6] method. Although our methodology to identify the LGN seed voxels might appear biased as it is already based on DTI information, we stress that the estimated LGN location and extent consistently fits known anatomy [28] and previous imaging reports [5]. Furthermore, this method is not prone to operator dependent seed selection. The comparison between streamline methods and our GCM technique illustrates the lower local sensitivity of the latter, since spatially close seeds lead to relatively similar connectivity maps, hence to close fibers tracts (figure 4). This can be an advantage over classical streamline approaches as it is less prone to noise, but might also obscure local topology across spatially close fibers, such as those shown by Conturo *et al.* in the thalamo-occipital fiber bundle [11].

### *Splenium fibers*

We investigated the topology of callosal fibers with respect to their origin in the low level visual cortex. We could reproduce with our GCM method the antero-ventral localization of fibers linking occipital retinotopic areas to the splenium (figure 5), as found by Dougherty *et al.* [15] using a classical streamline approach. Our results also suggest higher connectivity values for V3A when compared to V4, which is consistent with [15]. We could not however identify the precise topological organization of connections within the splenium they observed, neither with our GCM approach nor with a streamline technique similar to the one they used. A lower quality in our diffusion-weighted images may be responsible for this discrepancy.

We found the lowest connectivity values in the splenium for hMT+ as compared to occipital retinotopic areas (figure 5). This result should be related to a clinical study demonstrating that visual motion perception, strongly correlated with hMT+ activity, is not affected by posterior callosal destruction [8]. On the other hand, a weaker activation during bilateral visual field stimulation was found in the patient left hemisphere calcarine region compared to 20 normal subjects, correlated with severely impaired reading and color naming performances. These findings suggested other, probably parallel, pathways conveying interhemispheric visual motion information. Possible candidates proposed by the authors for the alternative routes include anterior part of the corpus callosum, anterior commissure and subcortical (via the superior colliculus, the intercollicular commissure and the pulvinar) connections. Future work will shortly assess these alternative interhemispheric connections for hMT+.

### *hMT+ and occipital areas connectivity*

We studied the connectivity between hMT+ and various low-level retinotopic areas. To the best of our knowledge, this is the first DTI connectivity study considering this cornerstone of the visual motion pathway. V1 systematically showed the highest connectivity index values with hMT+ (figure 7), consistent with the known highly myelinated white matter fiber bundles linking both areas [59]. Besides, lowest connectivity values between the retinotopic areas and hMT+ were systematically found

for area V4, further supporting the famous distinction between ventral and dorsal streams [56, 43]. We also found similar hMT+ connectivity values for V3d and V3v, despite their relatively important distance along the cortical sheet. This observation could be an other evidence to consider V3d and V3v as the two quarterfields representation of a single area V3, as also demonstrated with anatomical connectivity studies in various species of monkeys [40, 41].

#### *Hemisphere asymmetry*

Our results in the visual system suggested a significant asymmetry in our connectivity maps between the two hemispheres. The left hemisphere exhibits higher connectivity values than its right counterpart. A similar result was also reported in [15], where more occipito-callosal fibers could be reconstructed in the left than in the right hemisphere by the employed streamline algorithm. The authors suggested a bias in the hemispheres respective size may account for this difference. Note that such an asymmetry between both hemispheres was also reported in the motor system [26] and could possibly be attributed to handedness. Similarly, [24] reported a greater asymmetry in the left than in the right hemisphere in most parts of the cingulum, but no significant correlation with handedness could be demonstrated [23]. We suggest an alternative hypothesis, based on a perhaps more straightforward brain observation: hemispheric functional specialization. Undoubtedly, the hemispheres are functionally asymmetric and this should imply a different, asymmetrical wiring within each hemisphere. This may in particular be the case in the occipital cortex, the right lobe possibly presenting more fiber crossings than its left counterpart. As a consequence, the local diffusion tensors would not be equivalently anisotropic in both sides, leading to more difficult fiber tracking for streamline methods or lower connectivity values for our GCM algorithm.

## **5 Conclusion**

We evaluated the ability of a new geometric DTI analysis framework, GCM, to infer anatomical connectivity in the visual cortex. Our results confirm previous reports regarding the optic radiations and callosal fibers. We further give the first insights regarding hMT+ connections with occipital retinotopic areas.

## **6 Acknowledgments**

N.W. was supported by the French National Ministry of Research. C.L. was partly supported by a PACA region grant. We are grateful to Drs. M. Roth, B. Nazarian and J.-L. Anton for MRI scanner facilities.

## References

- [1] P.J. Basser, J. Mattiello, and D. LeBihan. MR diffusion tensor spectroscopy and imaging. *Biophysical Journal*, 66(1):259–267, 1994.
- [2] T.E.J. Behrens, M.W. Woolrich, M. Jenkinson, H. Johansen-Berg, R.G. Nunes, S. Clare, P.M. Matthews, J.M. Brady, and S.M. Smith. Characterization and propagation of uncertainty in Diffusion-Weighted MR Imaging. *Magnetic Resonance in Medicine*, 50:1077–1088, 2003.
- [3] J.S.W. Campbell, K. Siddiqi, V.V. Rymar, A. Sadikot, and B.G. Pike. Flow-based fiber tracking with diffusion tensor q-ball data: Validation and comparison to principal diffusion direction techniques. *NeuroImage*, 27(4):725–736, October 2005.
- [4] M. Catani, D.K. Jones, R. Donato, and D. H. ffytche. Occipito-temporal connections in the human brain. *Brain*, 126(9):2093–2107, September 2003.
- [5] W. Chen, X. Zhu, et al. Retinotopic mapping of lateral geniculate nucleus in humans using functional magnetic resonance imaging. *Proc. Natl. Acad. Sci. USA*, 96:2430–2434, March 1999.
- [6] O. Ciccarelli, G.J.M. Parker, A.T. Toosy, C.A.M. Wheeler-Kingshott, G.J. Barker, P.A. Boulby, D.H. Miller, and A.J. Thompson. From diffusion tractography to quantitative white matter tract measures: a reproducibility study. *NeuroImage*, 18(2):348–359, February 2003.
- [7] O. Ciccarelli, A.T. Toosy, G.J.M. Parker, C.A.M. Wheeler-Kingshott, G.J. Barker, D.H. Miller, and A.J. Thompson. Diffusion tractography based group mapping of major white-matter pathways in the human brain. *NeuroImage*, 19(4):1545–1555, August 2003.
- [8] S. Clarke, P. Maeder, R. Meuli, F. Staub, A. Bellmann, L. Regli, N. de Tribolet, and Assal G. Interhemispheric transfer of visual motion information after a posterior callosal lesion: a neuropsychological and fMRI study. *Experimental Brain Research*, 132(1):127–133, 2000.
- [9] S. Clarke and J. Miklossy. Occipital cortex in man: Organization of callosal connections, related myelo- and cytoarchitecture, and putative boundaries of functional visual areas. *The Journal of Comparative Neurology*, 298(2):188–214, 1990.
- [10] Y. Cointepas, J.-F. Mangin, Line Garnero, J.-B. Poline, and H. Benali. BrainVISA: Software platform for visualization and analysis of multi-modality brain data. In *Proc. 7th HBM*, page S98, Brighton, United Kingdom, 2001.
- [11] T.E. Conturo, N.F. Lori, T.S. Cull, E. Akbudak, A.Z. Snyder, J.S. Shimony, R.C. McKinstry, H. Burton, and M.E. Raichle. Tracking neuronal fiber pathways in the living human brain. *Proceedings of the National Academy of Sciences*, 96:10422–10427, August 1999.
- [12] A.M. Dale, B. Fischl, and M.I. Sereno. Cortical surface-based analysis I: Segmentation and surface reconstruction. *NeuroImage*, 9:179–194, 1999.

- [13] M. Descoteaux, E. Angelino, S. Fitzgibbons, and R. Deriche. A linear and regularized odf estimation algorithm to recover multiple fibers in q-ball imaging. Technical Report 5768, INRIA, November 2005.
- [14] M. Descoteaux, E. Angelino, S. Fitzgibbons, and R. Deriche. A fast and robust odf estimation algorithm in q-ball imaging. In *Third IEEE International Symposium on Biomedical Imaging: From Nano to Macro*, Arlington, Virginia, USA., April 2006.
- [15] R.F. Dougherty, M. Ben-Shachar, R. Bammer, A.A. Brewer, and B.A. Wandell. Functional organization of human occipital-callosal fiber tracts. *Proceedings of the National Academy of Science*, 102(20):7350–7355, May 2005.
- [16] S.P. Dukelow, J.F.X. DeSouza, J.C. Culham, A.V. Van Den Berg, R. Menon, and T. Vilis. Distinguishing subregions of the human MT+ complex using visual fields and pursuit eye movements. *Journal of Neurophysiology*, 86(4):1991–2000, October 2001.
- [17] S. Dumoulin, R. Bittar, N.J. Kabani, C.L. Baker, G. Le Goualher, G.B. Pike, and A.C. Evans. A new anatomical landmark for reliable identification of human area V5/MT: a quantitative analysis of sulcal patterning. *Cerebral Cortex*, 10:454–463, May 2000.
- [18] O. Faugeras, G. Adde, G. Charpiat, C. Chefid’Hotel, M. Clerc, T. Deneux, R. Deriche, G. Hermosillo, R. Keriven, P. Kornprobst, J. Kybic, C. Lenglet, L. Lopez-Perez, T. Papadopoulo, J.-P. Pons, F. Ségonne, B. Thirion, D. Tschumperlé, T. Viéville, and N. Wotawa. Variational, geometric, and statistical methods for modeling brain anatomy and function. *NeuroImage*, 23S1:S46–S55, 2004. Special issue: Mathematics in Brain Imaging - Edited by P.M. Thompson, M.I. Miller, T. Ratnanather, R.A. Poldrack and T.E. Nichols.
- [19] L.R. Frank. Anisotropy in high angular resolution diffusion-weighted mri. *Magnetic Resonance in Medicine*, 45:935–939, 2001.
- [20] L. Freire, A. Roche, and J.F. Mangin. What is the best similarity measure for motion correction in fMRI time series? *IEEE Transactions on Medical Imaging*, 21(5):470–484, May 2002.
- [21] O. Friman and C.F. Westin. Uncertainty in white matter fiber tractography. In *Proceedings of MICCAI*, pages 107–114. springer-verlag, 2005.
- [22] K.J. Friston, A.P. Holmes, J.B. Poline, P.J. Grasby, S.C. Williams, R.S. Frackowiak, and R. Turner. Analysis of fMRI time series revisited. *Neuroimage*, 2:45–53, 1995.
- [23] G. Gong, T. Jiang, C. Zhu, Y. Zang, Y. He, S. Xie, and J. Xiao. Side and handedness effects on cingulum from diffusion tensor imaging. *NeuroReport*, 16(15):1701–1705, 2005.
- [24] G. Gong, T. Jiang, C. Zhu, Y. Zang, F. Wang, S. Xie, J. Xiao, and X. Guo. Asymmetry analysis of cingulum based on scale-invariant parametrization by diffusion tensor imaging. *Human Brain Mapping*, 24(2):92–98, 2005.

- [25] K. Grill-Spector and R. Malach. The human visual cortex. *Annual Reviews Neuroscience*, 27:649–677, 2004.
- [26] M. Guye, G. J.M. Parker, M. Symms, P. Boulby, C.A.M. Wheeler-Kingshott, A. Salek-Haddadi, G.J. Barker, and J.S. Duncan. Combined functional MRI and tractography to demonstrate the connectivity of the human primary motor cortex in vivo. *NeuroImage*, 19:1349–1360, 2003.
- [27] K.M. Hasan, D.L. Parker, and A.L. Alexander. Magnetic resonance water self-diffusion tensor encoding optimization methods for full brain acquisition. *Image Analysis and Stereology*, 21(2):87–96, 2002.
- [28] J.C. Horton, K. Landau, P. Maeder, and W.F. Hoyt. Magnetic resonance imaging of the human lateral geniculate body. *Archives of Neurology*, 47(11):1201–1206, November 1990.
- [29] A. Huk, R. Dougherty, and D. Heeger. Retinotopy and functional subdivision of human areas MT and MST. *The Journal of Neuroscience*, 22(16):7195–7205, August 2002.
- [30] M. Jackowski, C.Y. Kao, M. Qiu, R.T. Constable, and L.H. Staib. White matter tractography by anisotropic wavefront evolution and diffusion tensors imaging. *Medical Image Analysis*, 9:427–440, 2005.
- [31] S. Jbabdi, P. Bellec, G. Marrelec, and H. Benali. A level set method for building anatomical connectivity paths between brain areas using DTI. In *Proceedings of ISBI*, pages 1024–1027, Arlington, VA, April 2004. IEEE, NIH.
- [32] P. Jezzard and R. S. Balaban. Correction for geometric distortions in echoplanar images from b0 field variations. *Magnetic Resonance in Medicine*, 34:65–73, 1995.
- [33] M. Lazar, D.M. Weinstein, J.S. Tsuruda, K.M. Hasan, K. Arfanakis, M.E. Meyerand, B. Badie, H.A. Rowley, V. Haughton, A. Field, and A.L. Alexander. White matter tractography using diffusion tensor deflection. In *Human Brain Mapping*, volume 18, pages 306–321, 2003.
- [34] D. Le Bihan. Looking into the functional architecture of the brain with diffusion mri. *Nature Reviews Neuroscience*, 4(6):469–480, 2003.
- [35] S. Lehericy, C. Lenglet, J. Doyon, H. Benali, P.F. Van de Moortele, G. Sapiro, O. Faugeras, R. Deriche, and K. Ugurbil. Activation shifts from the premotor to the sensorimotor territory of the striatum during the course of motor sequence learning. In *11th Annual Meeting of the Organization for Human Brain Mapping*, Toronto, June 2005.
- [36] C. Lenglet, R. Deriche, and O. Faugeras. Diffusion tensor magnetic resonance imaging: Brain connectivity mapping. Technical Report 4983, INRIA, November 2003.
- [37] C. Lenglet, R. Deriche, and O. Faugeras. Inferring white matter geometry from diffusion tensor MRI: Application to connectivity mapping. In T. Pajdla and J. Matas, editors, *Proceedings of the 8th European Conference on Computer Vision*, Prague, Czech Republic, May 2004. Springer-Verlag.

- [38] C. Lenglet, M. Rousson, R. Deriche, and O. Faugeras. Statistics on the manifold of multivariate normal distributions: Theory and application to diffusion tensor mri processing. *Journal of Mathematical Imaging and Vision*, 2006. In press.
- [39] Christophe Lenglet, Rachid Deriche, and Théo Papadopoulo. Implementation and evaluation of the adaptative estimation of gst. Technical report, Odysée - INRIA, May 2003.
- [40] D.C. Lyon and J.H. Kaas. Evidence for a modified V3 with dorsal and ventral halves in macaque monkeys. *Neuron*, 33:453–461, January 2002.
- [41] D.C. Lyon and J.H. Kaas. Evidence from V1 connections for both dorsal and ventral subdivisions of V3 in three species of new world monkeys. *Journal of Comparative Neurology*, 449(3):281–297, 2002.
- [42] J.-F. Mangin, C. Poupon, Y. Cointepas, D. Rivière, D. Papadopoulos-Orfanos, C. A. Clark, J. Régis, and D. Le Bihan. A framework based on spin glass models for the inference of anatomical connectivity from Diffusion-Weighted MR data. *NMR in Biomedicine*, 15:481–492, 2002.
- [43] A.D. Milner and M.A. Goodale. *The visual brain in action*. Oxford University Press, 1995.
- [44] S. Mori, B.J. Crain, V.P. Chacko, and P.C.M. Van Zijl. Three-dimensional tracking of axonal projections in the brain by Magnetic Resonance Imaging. *Annals of Neurology*, 45(2):265–269, February 1999.
- [45] L. O’Donnell, S. Haker, and C.F. Westin. New approaches to estimation of white matter connectivity in Diffusion Tensor MRI: Elliptic PDEs and geodesics in a tensor-warped space. In *MICCAI*, 2002. 459–466.
- [46] S. Ogawa, T.M. Lee, A.R. Kay, and D.W. Tank. Brain magnetic resonance imaging with contrast dependent on blood oxygenation. In *Proceedings of the National Academy of Sciences of the United States of America*, volume 87, pages 9868–9872, December 1990.
- [47] S. Osher. A level set formulation for the solution of the dirichlet problem for a hamilton-jacobi equations. *SIAM Journal on Mathematical Analysis*, 24(5):1145–1152, 1993.
- [48] E. Ozarslan, B. C. Vemuri, and T. Mareci. Fiber orientation mapping using generalized diffusion tensor imaging. In *ISBI*, pages 1036–1039, 2004.
- [49] G.J.M. Parker, K.E. Stephan, G.J. Barker, J.B. Rowe, D.G. MacManus, C.A.M. Wheeler-Kingshott, O. Ciccarelli, R.E. Passingham, R.L. Spinks, R.N. Lemon, and R. Turner. Initial demonstration of in vivo tracing of axonal projections in the macaque brain and comparison with the human brain using Diffusion Tensor Imaging and Fast Marching Tractography. *NeuroImage*, 15(4):797–809, April 2002.
- [50] G.J.M. Parker, C.A.M. Wheeler-Kingshott, and G.J. Barker. Estimating distributed anatomical connectivity using Fast Marching Methods and Diffusion Tensor Imaging. *Trans. Med. Imaging*, 21(5):505–512, 2002.

- [51] C. Pierpaoli, P. Jezzard, P.J. Basser, A. Barnett, and G. Di Chiro. Diffusion Tensor MR imaging of human brain. *Radiology*, 201:637–648, 1996.
- [52] E. Prados, C. Lenglet, J.P. Pons, N. Wotawa, R. Deriche, O. Faugeras, and S. Soatto. Control theory and fast marching methods for brain connectivity mapping. In *Proc. IEEE Computer Society Conference on Computer Vision and Pattern Recognition*, New York, NY, June 2006.
- [53] J.A. Sethian. *Level Set Methods*. Cambridge University Press, 1996.
- [54] D. Tuch. Q-ball imaging. *Magnetic Resonance in Medicine*, 52(6):1358–1372, 2004.
- [55] C.W. Tyler, L.T. Likova, L.L. Konsevich, M.M. Schira, and A.R. Wade. Enhanced concepts of occipital retinotopy. *Current Medical Imaging Reviews*, 1:319–329, 2005.
- [56] L.G. Ungerleider and M. Mishkin. *Two cortical visual systems.*, pages 549–586. MIT Press, 1982.
- [57] D.C. Van Essen. A tension-based theory of morphogenesis and compact wiring in the central nervous system. *Nature*, 385:313–318, January 1997.
- [58] D.C. Van Essen, H.A. Drury, J. Dickson, J. Harwell, D. Hanlon, and C.H. Anderson. An integrated software suite for surface-based analyses of cerebral cortex. *Journal of American Medical Informatics Association*, 8:443–459, 2001.
- [59] D.C. Van Essen, J.H.R. Maunsell, and J.L. Bixby. The Middle Temporal visual area in the macaque: myeloarchitecture, connections, functional properties and topographic organization. *Journal of Comparative Neurology*, 199:293–326, 1981.
- [60] B.A. Wandell, A.A. Brewer, and R.F. Dougherty. Visual field map clusters in human cortex. *Phil. Trans. of the Royal Society London*, 360:693–707, 2005.
- [61] J. Watson, R. Myers, R. Frackowiak, J. Hajnal, R. Woods, J. Mazziotta, S. Shipp, and S. Zeki. Area V5 of the human brain: evidence from a combined study using Positron Emission Tomography and Magnetic Resonance Imaging. *Cerebral Cortex*, 3:79–94, 1993.
- [62] D.J. Werring, C.A. Clark, G.J.M. Parker, D.H. Miller, A.J. Thompson, and G.J. Barker. A direct demonstration of both structure and function in the visual system: combining Diffusion Tensor Imaging with functional Magnetic Resonance Imaging. *NeuroImage*, 9:352–361, 1999.
- [63] N. Wotawa, J.-P. Pons, L. Lopez, R. Deriche, and O. Faugeras. fMRI data smoothing constrained to the cortical surface: a comparison of the level-set and mesh-based approaches. In *NeuroImage (HBM'04)*, 2004.
- [64] N. Wotawa, B. Thirion, E. Castet, J.L. Anton, and O. Faugeras. Human retinotopic mapping using fMRI. Technical Report 5472, INRIA, January 2005.

## **Contents**

<b>1</b>	<b>Introduction</b>	<b>3</b>
<b>2</b>	<b>Methods</b>	<b>5</b>
<b>3</b>	<b>Results</b>	<b>14</b>
<b>4</b>	<b>Discussion</b>	<b>20</b>
<b>5</b>	<b>Conclusion</b>	<b>23</b>
<b>6</b>	<b>Acknowledgments</b>	<b>23</b>



---

Unité de recherche INRIA Sophia Antipolis  
2004, route des Lucioles - BP 93 - 06902 Sophia Antipolis Cedex (France)

Unité de recherche INRIA Futurs : Parc Club Orsay Université - ZAC des Vignes  
4, rue Jacques Monod - 91893 ORSAY Cedex (France)

Unité de recherche INRIA Lorraine : LORIA, Technopôle de Nancy-Brabois - Campus scientifique  
615, rue du Jardin Botanique - BP 101 - 54602 Villers-lès-Nancy Cedex (France)

Unité de recherche INRIA Rennes : IRISA, Campus universitaire de Beaulieu - 35042 Rennes Cedex (France)

Unité de recherche INRIA Rhône-Alpes : 655, avenue de l'Europe - 38334 Montbonnot Saint-Ismier (France)

Unité de recherche INRIA Rocquencourt : Domaine de Voluceau - Rocquencourt - BP 105 - 78153 Le Chesnay Cedex (France)

---

Éditeur

INRIA - Domaine de Voluceau - Rocquencourt, BP 105 - 78153 Le Chesnay Cedex (France)

<http://www.inria.fr>

ISSN 0249-6399